EES Catalysis

PAPER

Check for updates

Fe-modified CoCr layered double hydroxides for boosting the seawater oxygen evolution reaction

Edmond Nasr, Paul Byaruhanga, Dezhi Wang, Shuo Chen, [ID] Luo Yu* and Zhifeng Ren [ID] *

The development of efficient and stable oxygen evolution reaction (OER) electrocatalysts for seawater electrolysis is vital to enable sustainable hydrogen production in coastal and arid regions without further burdening scarce freshwater resources. Here, we report the design of an iron-modified cobalt–chromium layered double hydroxide (Fe–CoCr LDH) derived from a cobalt-based metal–organic framework (Co MOF) for the OER in alkaline seawater media. The synthesis was carried out entirely at room temperature using a rapid, solution-based process. The resulting Fe–CoCr LDH catalyst demonstrates high OER activity, achieving low overpotentials of 250, 300, and 320 mV at current densities of 100, 500, and 1000 mA cm^{-2}, respectively. Furthermore, the catalyst exhibits very good long-term stability in both 1 M KOH and 6 M KOH natural seawater, maintaining performance over 100 hours at 100 and 500 mA cm^{-2}. These results highlight the potential of earth-abundant transition metal-based LDHs as efficient OER electrocatalysts for seawater electrolysis applications.

Broader context

The transition to a carbon-neutral energy economy hinges on the ability to produce clean hydrogen using abundant and sustainable resources. While water electrolysis is a promising pathway for green hydrogen production, its large-scale implementation is constrained by freshwater scarcity in many parts of the world. Seawater, which constitutes over 96% of the Earth's water reserves, represents an attractive alternative feedstock, yet its complex ionic composition poses significant challenges for catalyst durability and selectivity, particularly at the anode, where the chlorine evolution reaction and corrosion affect performance. In this study, we present a simple and scalable strategy to design a highly active and corrosion-resistant oxygen evolution reaction (OER) electrocatalyst based on an Fe modified CoCr layered double hydroxide (LDH). The catalyst, synthesized *via* a room-temperature method from a Co MOFs precursor, exhibits excellent OER activity and stability in natural seawater, even at industrial current densities. When coupled with a NiMoN hydrogen evolution reaction catalyst, the full electrolyzer achieves high-efficiency overall water splitting with prolonged operational stability in concentrated alkaline seawater. Our findings offer a practical route toward low-cost, high performance electrocatalytic systems for seawater electrolysis, with direct implications for decentralized hydrogen production in water stressed regions.

Introduction

Hydrogen is widely recognized as a key component of the future sustainable energy landscape due to its high gravimetric energy density and environmental compatibility.[1–4] However, the sustainability of hydrogen as an energy carrier is inherently tied to the method of its production.[5–8] Currently, most hydrogen is produced *via* steam methane reforming and coal gasification, processes that emit large amounts of carbon dioxide, contributing to climate change and environmental degradation. In contrast, water electrolysis offers a carbon-free route to hydrogen generation, especially when powered by renewable

energy sources. This process involves two half-reactions: the hydrogen evolution reaction (HER) at the cathode and the oxygen evolution reaction (OER) at the anode.[9–11] Among these, the OER is kinetically sluggish and requires efficient electrocatalysts to drive the reaction at industrially relevant rates. While noble metal-based catalysts, such as IrO_2 and RuO_2, exhibit good OER activity, their high cost and limited availability pose significant barriers to widespread deployment.[12–15] Therefore, the development of low-cost, earth-abundant, and high-performance OER electrocatalysts is imperative for the scalable implementation of green hydrogen technologies.

Seawater, which accounts for approximately 96% of the Earth's water resources, represents an abundant and virtually inexhaustible alternative for hydrogen production.[16–18] This makes seawater electrolysis particularly advantageous for regions with limited access to freshwater. However, this approach

Department of Physics and Texas Center for Superconductivity at the University of Houston (TcSUH), University of Houston, Houston, TX 77204, USA.
E-mail: lyu2@central.uh.edu, zren@uh.edu

presents significant challenges at both the anode and cathode.[19,20] On the anode side, the chlorine evolution reaction (ClER) competes with the OER. Fortunately, in alkaline media, the OER is thermodynamically more favorable, with the onset potential approximately 480 mV lower than that of the ClER.[17,21] Designing highly active OER electrocatalysts capable of operating at industrially relevant current densities is critical to minimize overpotentials and suppress the parasitic ClER.[22] In addition, the presence of chloride ions in seawater introduces serious corrosion risks, especially for transition metal-based catalysts and substrates. These ions can accelerate structural degradation, leading to a reduced catalytic lifetime and performance decay.[23] Therefore, developing robust OER electrocatalysts that combine high activity, ClER suppression, and excellent resistance to chloride-induced corrosion is a key objective in the advancement of seawater electrolysis.[24]

Cobalt-based metal–organic frameworks (Co MOFs) are highly attractive precursors for OER electrocatalysts due to their uniform metal dispersion, large surface area, and structural tunability.[25] These MOFs can be transformed into a range of functional materials, such as oxides,[26] sulfides,[27] tellurides,[28] phosphides,[29] nitrides,[30] and layered double hydroxides (LDHs),[22] depending on the treatment conditions. Among these derivatives, LDHs offer considerable advantages for electrocatalysis, including high compositional flexibility and tunable chemistry. Although Co-based LDHs have been widely studied, CoCr LDHs have received less attention, primarily due to their moderate OER performance.[31] However, recent studies reveal a synergistic interplay between cobalt and chromium ions that can be leveraged to boost OER kinetics. Mechanistic investigations show that Co^{2+} serves as the primary active site, undergoing oxidation to β-CoOOH during the OER, while Cr^{3+} functions as a charge mediator, enhancing conductivity and promoting efficient electron transfer across the LDH lattice.[32] Further studies indicate that Cr^{3+} may be oxidized *in situ* to Cr^{6+} during anodic polarization, generating additional active sites and contributing to the stabilization of the catalytic structure.[32] To further enhance the performance of CoCr LDHs, multiple strategies have been employed to modulate their electronic structure. One approach involves lattice doping with single Ru atoms, which has been shown to modulate the electronic structure of Co sites, enhance charge transfer, and optimize the adsorption energies of key OER intermediates (O*, OH*, and OOH*).[33] Another effective strategy involves the introduction of vanadium as a third metal, forming layered triple hydroxides (LTHs).[34] This structural modification not only introduces additional redox-active sites but also promotes the electronic interaction between Co^{2+} and V^{5+}, which facilitates charge transfer and enhances hydroxide adsorption. The resulting CoCrV LTH catalysts exhibit superior OER activity and stability in both alkaline freshwater and seawater electrolytes. These findings underscore the potential of rationally designed multi-metallic CoCr-based LDHs as efficient and corrosion-resistant electrocatalysts for water oxidation, particularly in challenging saline environments.

In this work, we developed a high-performance OER catalyst consisting of an Fe-modified CoCr layered double hydroxide (Fe–CoCr LDH) synthesized *via* a straightforward chemical transformation of Co MOFs on nickel foam. The synthesis involved a one-step coprecipitation process in a mixed solution of Fe^{2+} and Cr^{3+} salts, resulting in a uniform nanosheet array morphology with enhanced surface area and porosity. Remarkably, the Fe–CoCr LDH catalyst achieved low overpotentials of 200, 250, and 300 mV at current densities of 10, 100, and 500 mA cm^{-2}, respectively, in 1 M KOH, outperforming both the pristine Co MOFs and CoCr LDH, as well as the commercial IrO_2 benchmark. Furthermore, when coupled with a good HER catalyst NiMoN in a two-electrode configuration, the Fe–CoCr LDH//NiMoN system demonstrated very good overall water splitting performance in both alkaline freshwater and alkaline seawater environments, exhibiting activity superior to that of many recently reported systems. These results highlight the effectiveness of our Fe modification strategy and underscore the potential of Fe–CoCr LDH as a robust electrocatalyst for seawater electrolysis.

Results and discussion

As shown in Fig. 1A, our Fe–CoCr LDH catalyst was obtained from Co MOFs grown on nickel foam through a room-temperature coprecipitation process. A distinct color change from violet (Co MOFs) to earthy brown (Fe–CoCr LDH) was observed, indicating successful phase transformation. This transformation is further visually confirmed by the optical images shown in Fig. S1 of the SI, which clearly show the color transition from Co MOFs to Fe–CoCr LDH. Impressively, this synthesis approach provides good scalability, which was demonstrated by the successful preparation of a 5 cm × 5 cm sample with a uniform color across the entire surface, as shown in Fig. S2, and comparable OER activity to that of the small-scale samples (Fig. S3). Scanning electron microscopy (SEM) images reveal that the surface of the Ni foam was uniformly covered with vertically aligned nanosheet arrays following Co MOFs growth, with each sheet having an average thickness of approximately 600 nm (Fig. 1B and C). As shown in Fig. S4, the bare Ni foam exhibits a relatively smooth surface with no nanosheet features, confirming that the observed architecture arises from the MOFs growth process. In the second step, one piece of the Co MOFs/Ni foam was immersed in an aqueous solution containing $FeSO_4$ and $Cr(NO_3)_3$ to produce the final Fe–CoCr LDH catalyst. This transformation follows an etching–incorporation–sedimentation mechanism.[35,36] The $FeSO_4$ and $Cr(NO_3)_3$ solution forms a weakly acidic environment through the hydrolysis of Fe^{2+} and Cr^{3+} ions. Simultaneously, Co^{2+} species undergo a reversible hydrolysis process, generating $Co(OH)_2$ and H^+ ions.[36] The accumulation of H^+ ions initiates the breakdown of coordination bonds between the Co centers and organic linkers in the MOFs, effectively etching the framework. As hydrolysis continues, Cr^{3+}, Fe^{2+}, and Co^{2+} precipitate as their respective metal hydroxides. These hydroxides then undergo co-sedimentation on the Ni foam surface to form the LDH phase. Finally, Cr and Fe are incorporated into the
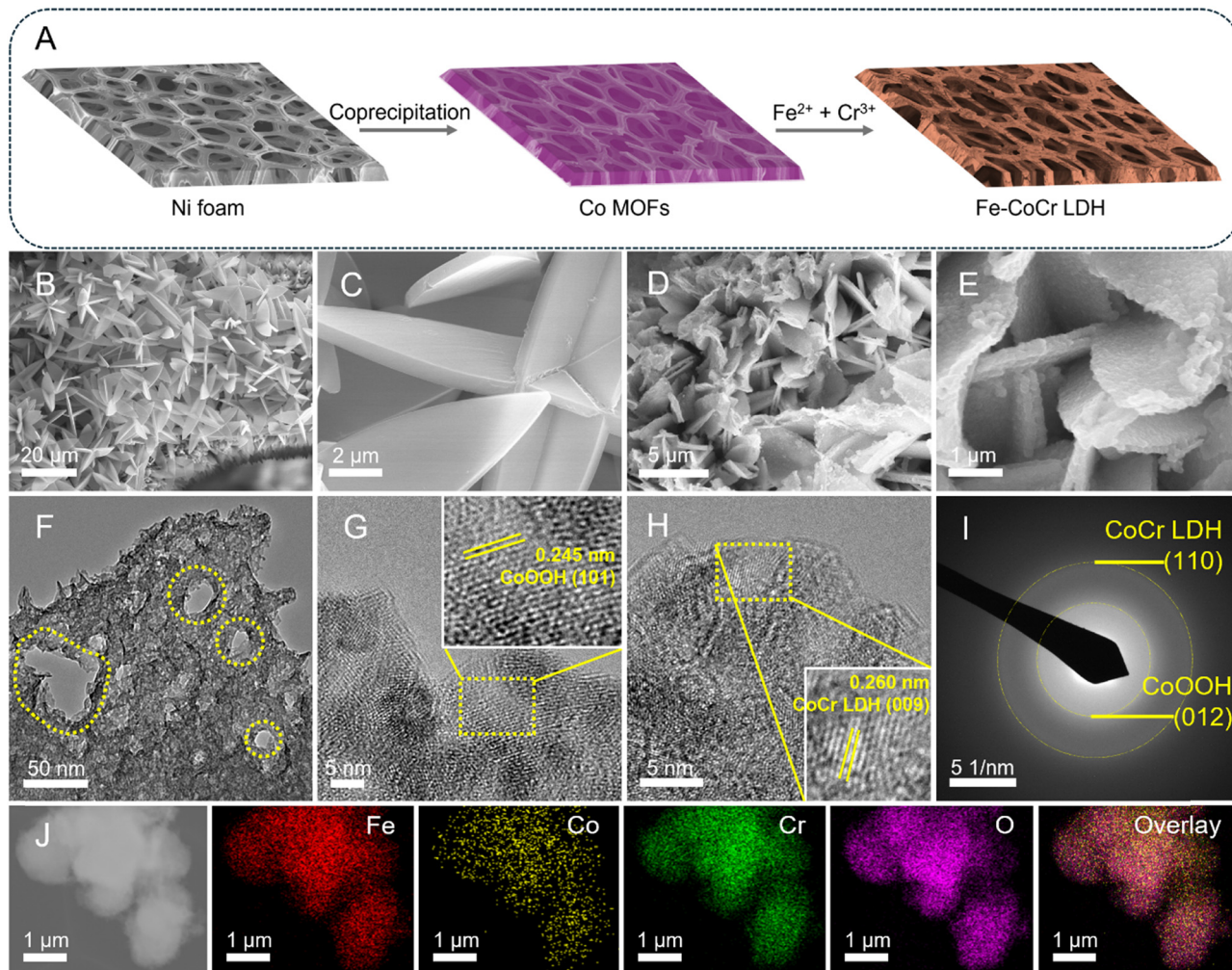
Fig. 1 Catalyst synthesis and characterization. (A) Schematic illustration of the synthesis process for the Fe−CoCr LDH electrocatalyst. (B) and (C) SEM images of Co MOFs. (D) and (E) SEM images, (F) TEM image, (G and H) HRTEM images, (I) SAED pattern, and (J) ADF-STEM image and corresponding elemental mapping images of Fe−CoCr LDH.

Co-based LDH through anion exchange, resulting in the formation of a multimetallic Fe–CoCr LDH catalyst.[37] SEM images (Fig. S5) further show that CoCr LDH synthesized without iron loses the nanosheet structure exhibited by the Co MOFs, suggesting collapse of the MOF-derived morphology during transformation. In contrast, the Fe modified sample retains this morphology. This is an effect attributed to the presence of Fe^{2+}, which partially neutralizes the strong acidity of the Cr^{3+} solution, leading to a milder etching environment that helps preserve structural integrity. SEM images (Fig. 1D and E) of Fe–CoCr LDH reveal a nanosheet array morphology similar to that of the Co MOFs. However, after the etching and transformation process, the LDH material exhibits increased surface roughness on the nanosheets, indicating successful structural modification. These observations confirm that the coprecipitation process yields a uniformly distributed nanosheet architecture across the Ni foam substrate, along with a large surface area beneficial for electrochemical reactions. The transmission electron microscopy (TEM) image in Fig. 1F reveals the high

degree of roughness on the surface of each nanosheet, as well as the clearly visible extensive internal porosity marked by yellow dashed circles. These observations are further supported by additional TEM and high-resolution transmission electron microscopy (HRTEM) images of Fe–CoCr LDH in the SI (Fig. S6), which reveal internal mesoporous structures throughout the nanosheets marked by yellow dashed circles. HRTEM images in Fig. 1G and H reveal two distinct lattice fringes with interplanar spacings of 0.245 nm and 0.260 nm, corresponding to the (101) plane of CoOOH and the (009) plane of CoCr LDH, respectively. Additionally, the selected area electron diffraction (SAED) pattern in Fig. 1I displays two prominent diffraction rings, which are indexed to the (110) plane of CoCr LDH and the (012) plane of CoOOH. An annular dark-field scanning TEM (ADF-STEM) image and associated elemental mapping images (Fig. 1J) further confirm the homogeneous distribution of Co, Cr, Fe, and O throughout the nanosheet arrays, validating the successful incorporation of Fe into the CoCr LDH framework.

To determine the exact composition of the catalyst, X-ray diffraction (XRD) analysis was performed on Fe–CoCr LDH. As shown in Fig. 2A, in addition to the three characteristic peaks originating from the Ni foam, a weak peak at 20.23° was observed and indexed to the (003) plane of CoOOH (PDF# 07-0169) and another at 22.60°, corresponding to the (006) plane of CoCr LDH.[31] The presence of these peaks confirms the successful conversion of the Co MOFs precursor into a LDH structure. Importantly, the coexistence of CoOOH is catalytically beneficial. A growing body of evidence identifies CoOOH as an active species for oxygen evolution. For example, nanocrystalline, hydrated β-CoOOH films have been shown to exhibit high activity by enabling efficient hydroxyl ion transport and exposing additional active sites at grain boundaries.[38] Operando investigations further confirm that Co-based oxides and hydroxides undergo in situ transformation into CoOOH under OER conditions, with Fe incorporation lowering the energy barrier for oxygen evolution and optimizing the adsorption of OER intermediates.[39,40]

Taken together, these findings establish that CoOOH not only is a catalytically active species but also benefits from Fe-induced electronic tuning, features directly relevant to our Fe-modified CoCr LDH system.

X-ray photoelectron spectroscopy (XPS) was employed to investigate the oxidation states of Fe–CoCr LDH and CoCr LDH. The high-resolution Fe 2p spectrum of Fe–CoCr LDH (Fig. 2B) shows two distinct peaks at 713.3 eV (Fe $2p_{3/2}$) and 724.5 eV (Fe $2p_{1/2}$), along with two satellite (denoted as Sat.) peaks at 717.2 eV and 731.9 eV. These features are characteristic of Fe^{3+} species, confirming that iron exists predominantly in the trivalent state.[41] In the Co 2p region (Fig. 2C), the spectra of CoCr LDH and Fe–CoCr LDH show two main spin–orbit peaks at 781.9 eV (Co $2p_{3/2}$) and 798.9 eV (Co $2p_{1/2}$), along with accompanying satellite peaks, indicating the coexistence of both Co^{2+} and Co^{3+} oxidation states.[42] Importantly, no

significant shift was observed in the Co 2p peaks after iron incorporation, suggesting that the Co chemical environment remained largely unchanged. In contrast, the Cr 2p spectrum displays a clear shift following Fe modification. As shown in Fig. 2D, for the pristine CoCr LDH, the Cr $2p_{3/2}$ and Cr $2p_{1/2}$ peaks are located at 578.0 eV and 587.8 eV, respectively, consistent with the Cr^{3+} oxidation state. Two additional low-intensity peaks at 579.5 eV and 589.3 eV are attributed to shake-up satellite peaks, commonly observed for Cr^{3+} systems.[43] After Fe modification, both Cr peaks shift by approximately 0.5 eV to lower binding energies (577.5 eV and 587.3 eV, respectively), indicating an increase in electron density around the Cr centers, which is favorable for the OER.[32–34,44] Additionally, the high-resolution O 1s spectra of CoCr LDH and Fe–CoCr LDH (Fig. S7) feature two peaks at 532.1 eV and 533.4 eV, attributed to metal–OH and adsorbed H_2O species, respectively.[45–47]

We first evaluated the electrocatalytic OER activity of our catalysts in 1 M KOH using a standard three-electrode system. As shown in Fig. 3A, the Fe-modified CoCr LDH exhibits the best OER performance among the different catalysts, including the benchmark IrO_2. It achieves low overpotentials of 200, 250, and 300 mV at current densities of 10, 100, and 500 mA cm^{-2}, respectively. To further assess the reaction kinetics, we analyzed the corresponding Tafel slopes. As shown in Fig. 3B, the Fe–CoCr LDH catalyst demonstrates the lowest Tafel slope of 36.8 mV dec^{-1}, confirming its superior OER activity and efficient kinetics. Furthermore, to optimize the catalyst's performance, we systematically examined the effects of the reaction time and Fe^{2+} ($FeSO_4·7H_2O$) concentrations during the second synthesis step on the catalytic activity (Fig. S8). Catalytic activity was found to decrease when the reaction time was either too short or too long, but the difference among them is small, which is even better for large-scale production, and a similar trend was observed for the Fe^{2+} concentration. Given its excellent performance in 1 M KOH, we investigated the potential of our Fe–CoCr LDH catalyst in alkaline seawater electrolysis. According to the Pourbaix diagram, the difference between the onset potentials of the OER and the competing ClER reaches a maximum ($\sim$480 mV) when the electrolyte pH exceeds 7.5, providing a favorable window for the selective OER. Thus, we tested the Fe–CoCr LDH catalyst in various alkaline simulated and natural seawater electrolytes. Fig. 3C presents polarization curves representing the catalyst's performance in 1 M KOH, 1 M KOH + 0.5 M NaCl, 1 M KOH + 1.5 M NaCl, 1 M KOH + Natural Seawater, and 6 M KOH + Natural Seawater. As indicated by the overpotentials at different current densities shown in Fig. 3D, the Fe–CoCr LDH catalyst has similar performance in all of the simulated and natural seawater electrolytes studied, with overpotentials at 500 mA cm^{-2} well below the ClER threshold of 480 mV. More impressively, in the highly alkaline and corrosive 6 M KOH + Natural Seawater electrolyte, the catalyst achieves further enhanced OER activity, delivering overpotentials of only 180, 240, and 280 mV at 10, 100, and 500 mA cm^{-2}, respectively.

To gain insight into the enhanced activity, we performed electrochemical impedance spectroscopy (EIS), as shown in Fig. 3E.
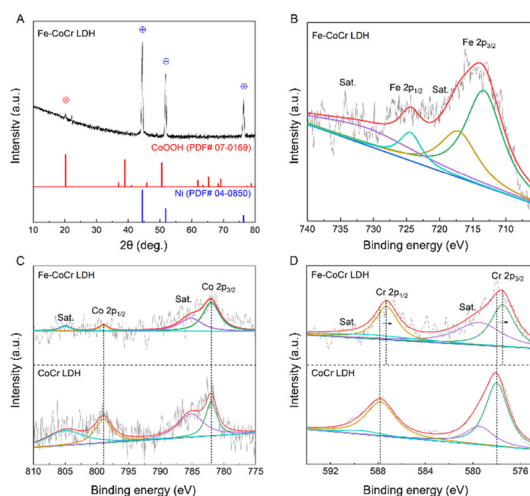
Fig. 2 (A) XRD patterns of Fe–CoCr LDH on Ni foam in comparison with those of standard CoOOH (red line PDF no. 07-0169) and Ni (blue line PDF no. 04-0850). High-resolution XPS spectra of (B) Fe 2p for Fe–CoCr LDH and (C) Co 2p and (D) Cr 2p for CoCr LDH and Fe–CoCr LDH.
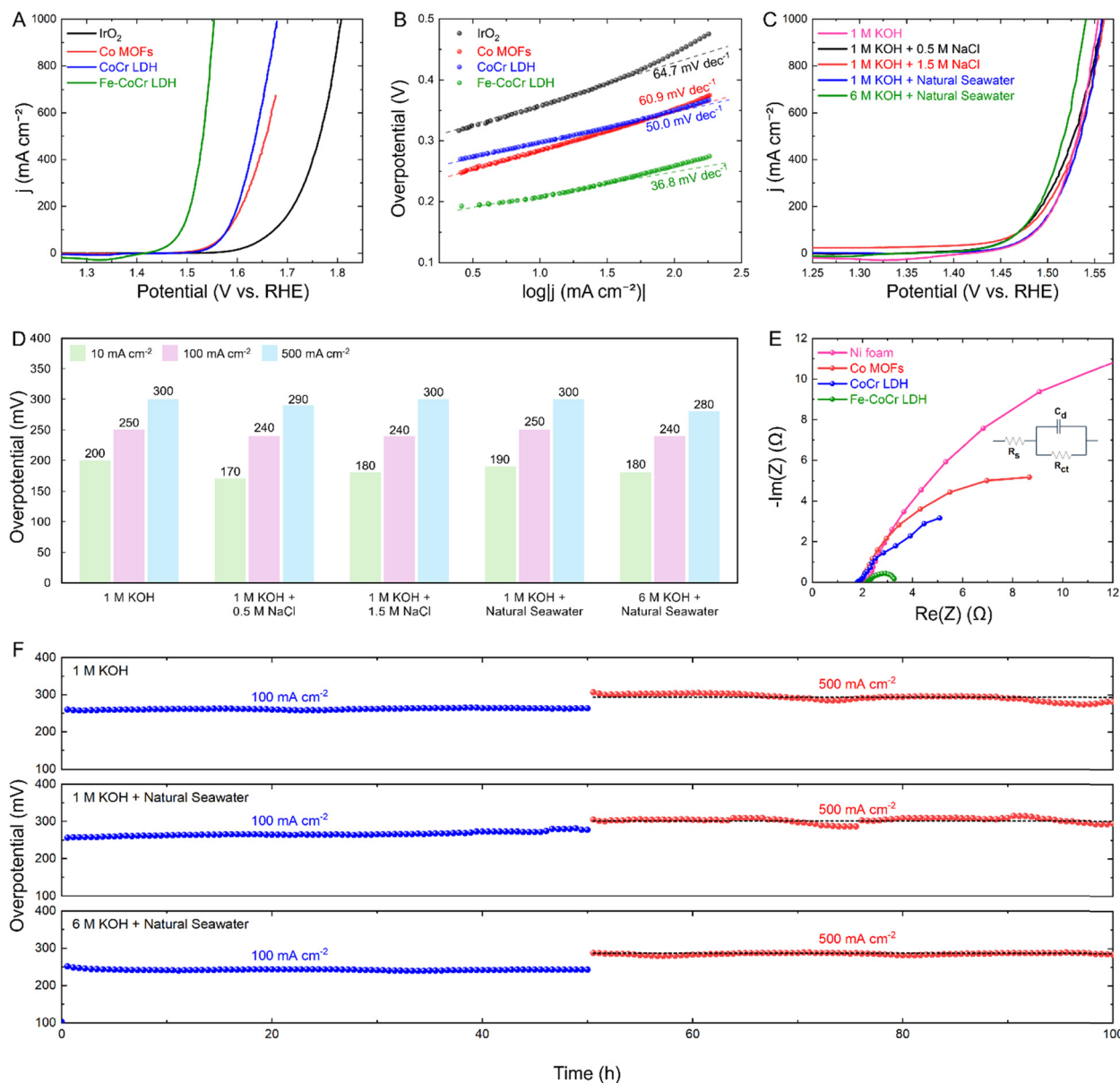
Fig. 3 (A) OER polarization curves for different catalysts in 1 M KOH. (B) Tafel slopes derived from the results shown in (A). (C) OER polarization curves for Fe–CoCr LDH in different electrolytes. (D) Grouped column chart based on the results in (C) showing the overpotential values required to achieve current densities of 10, 100, and 500 mA cm^{-2} in different electrolytes. (E) EIS Nyquist plots for different catalysts. Inset: The equivalent circuit. (F) Long-term stability testing of Fe–CoCr LDH in different electrolytes for 50 hours at a current density of 100 mA cm^{-2} followed by an additional 50 hours at a higher current density of 500 mA cm^{-2}.

The Fe–CoCr LDH catalyst exhibits a charge transfer resistance (R_{ct} = 3.2 Ω) lower than that of CoCr LDH (R_{ct} = 9.3 Ω), Co MOFs (R_{ct} = 15.2 Ω), and bare Ni foam (R_{ct} = 65.5 Ω), indicating significantly improved charge transport due to Fe incorporation. These observations are consistent with previous studies, which have shown that introducing Fe into layered hydroxide systems reduces charge transfer resistance and accelerates charge transport, thereby boosting catalytic efficiency.[48,49] Beyond enhanced conductivity, Fe incorporation is also known to modulate the electronic structure of neighboring Co and Cr sites, thereby tuning the adsorption energetics of OER intermediates and

improving intrinsic activity.[50–53] In addition, Fe species can serve directly as active centers, promoting the stabilization of high-valent intermediates that sustain OER catalysis under operating conditions.[48,50] Taken together, these synergistic effects contribute to the excellent OER performance of Fe–CoCr LDH in alkaline seawater. To further explore the origin of the improved OER activity, we evaluated the electrochemical active surface area (ECSA) of different catalysts by determining the double-layer capacitance (C_{dl}) *via* cyclic voltammetry at various scan rates. As shown in Fig. S9, the C_{dl} values for Co MOFs, CoCr LDH, and Fe–CoCr LDH are 1.02, 1.28, and 1.60 mF cm^{-2},
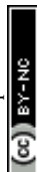
respectively, indicating that the iron-modified catalyst exhibits the highest ECSA. Furthermore, the ECSA-normalized polarization curves (Fig. S10) confirm the superior intrinsic OER activity of Fe–CoCr LDH. Interestingly, after normalizing the current density by the ECSA, Fe–CoCr LDH still shows the highest intrinsic activity among the catalysts studied. To further probe the intrinsic activity, we calculated the turnover frequency (TOF) for Fe–CoCr LDH, CoCr LDH, and Co MOFs. As shown in Fig. S11, Fe–CoCr LDH exhibits the highest TOF values

across the measured potential range, further demonstrating its enhanced intrinsic OER activity. Finally, we evaluated the long-term stability of Fe–CoCr LDH in 1 M KOH, 1 M KOH + Natural Seawater, and 6 M KOH + Natural Seawater. As shown in Fig. 3F, the catalyst was subjected to continuous operation for 50 hours at 100 mA cm^{-2}, followed by an additional 50 hours at 500 mA cm^{-2}. It is clear that the current density remains stable across all electrolytes, including the harsh 6 M KOH + Natural Seawater condition, demonstrating the catalyst's excellent
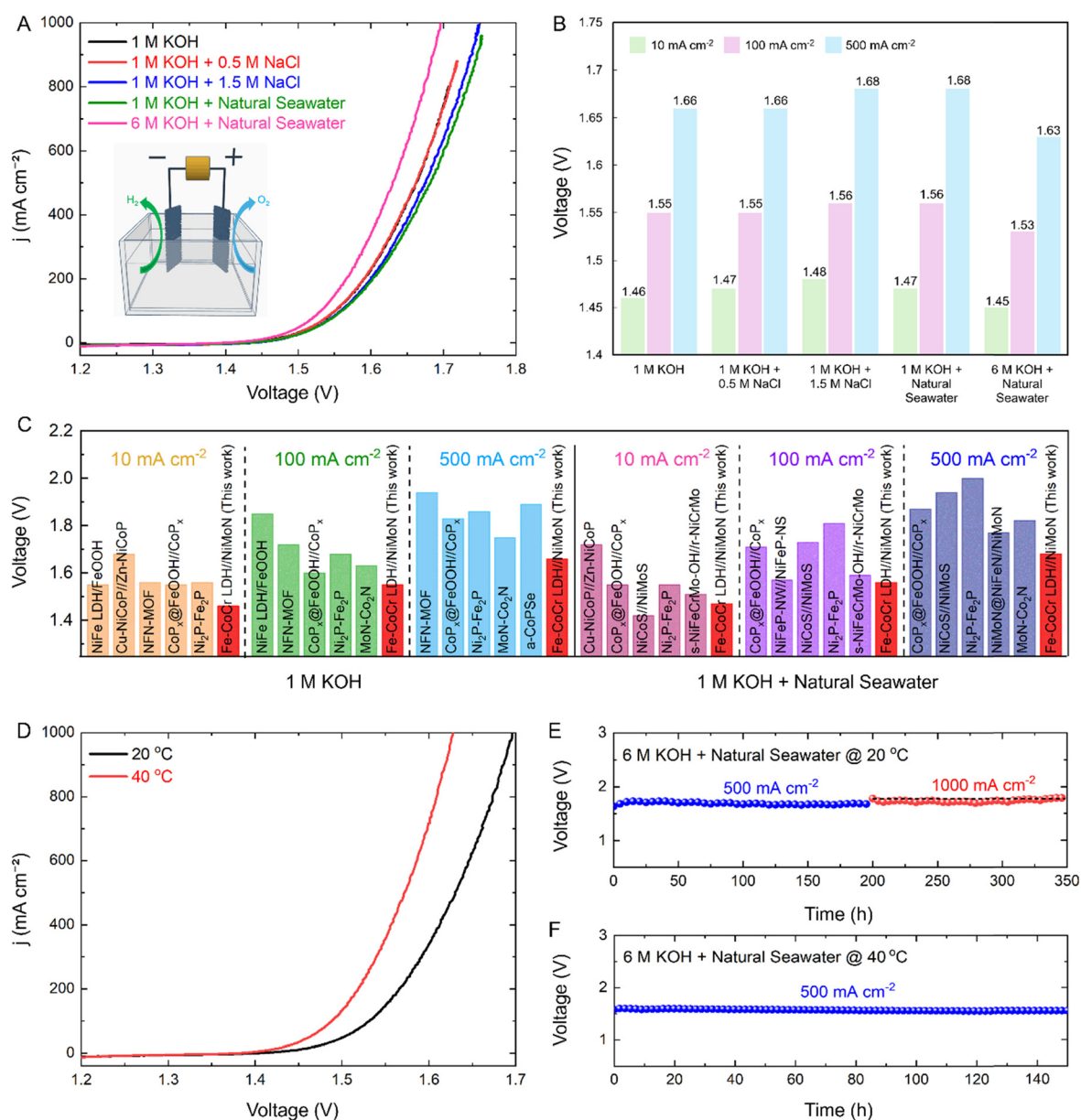
Fig. 4 (A) Overall water splitting performance of Fe–CoCr LDH//NiMoN in different electrolytes at room temperature. Inset: Schematic illustration of the 2-electrode configuration cell. (B) Grouped column chart based on the results in (A) showing the voltage values at current densities of 10, 100 and 500 mA cm^{-2}. (C) Grouped column chart showing comparisons of overall water splitting performance at current densities of 10, 100 and 500 mA cm^{-2} in different electrolytes between Fe–CoCr LDH//NiMoN and previously reported electrocatalysts in the 2-electrode configuration. (D) Overall water splitting performance of Fe–CoCr LDH//NiMoN in 6 M KOH + Natural Seawater at different temperatures. Long-term stability testing of Fe–CoCr LDH// NiMoN in 6 M KOH + Natural Seawater at (E) room temperature performed for 200 hours at 500 mA cm^{-2} followed by an additional 150 hours at 1000 mA cm^{-2} and (F) 40 °C performed for 150 hours at 500 mA cm^{-2}.

operational durability and stability under harsh conditions. To evaluate the structural durability of the catalyst, we carried out post-stability characterization studies after long-term electrolysis in 1 M KOH + Natural Seawater. Both the SEM (Fig. S12) and TEM results (Fig. S13) reveal that, although partial loss of nanosheets occurred during the prolonged operation, the overall nanosheet architecture and surface roughness were largely preserved. This observation confirms that the Fe–CoCr LDH catalyst maintains its nanosheet framework under harsh operating conditions, thereby ensuring sufficient exposure of active sites and sustained electrochemical performance. In addition, the chemical structure of Fe–CoCr LDH was also preserved without any changes (Fig. S13), demonstrating good structural stability. To further evaluate the corrosion resistance of the catalysts, corrosion polarization measurements were carried out in natural seawater. The corrosion potential (E_{corr}) and corrosion current density (j_{corr}) provide key indicators of intrinsic corrosion-resistance of a material.[54,55] As summarized in Fig. S14, Co MOFs exhibit E_{corr} = 0.268 V $vs.$ RHE and j_{corr} = 0.27 mA cm^{-2}, while CoCr LDH exhibits E_{corr} = 0.251 V $vs.$ RHE and j_{corr} = 0.06 mA cm^{-2}. In contrast, Fe–CoCr LDH displays a more positive E_{corr} of 0.377 V $vs.$ RHE and a lower j_{corr} of 0.054 mA cm^{-2}. The higher E_{corr} and lower corrosion j_{corr} clearly indicate that Fe incorporation enhances resistance to chloride-induced corrosion.

After confirming the high OER performance of Fe–CoCr LDH, we paired it with a good HER catalyst NiMoN in a two-electrode configuration (Fe–CoCr LDH//NiMoN) to evaluate the overall water splitting performance under various electrolytes at room temperature, as shown in Fig. 4A. Fig. 4B summarizes the cell voltages at different current densities for the various electrolytes. In both 1 M KOH and 1 M KOH + 0.5 M NaCl, the system exhibited comparable performance, achieving voltages of 1.55 V and 1.66 V at 100 and 500 mA cm^{-2}, respectively. The slightly higher cell voltages observed in 1 M KOH + 1.5 M NaCl arise from degradation of the NiMoN cathode in chloride-containing electrolytes, rather than from the Fe–CoCr LDH anode. This explanation is supported by additional HER measurements of NiMoN in both electrolytes (Fig. S15), which confirm its reduced activity in the presence of high concentrations of chloride ions. In more chemically challenging environments, such as 6 M KOH + Natural Seawater, it showed a slight improvement, reaching 1.63 V at 500 mA cm^{-2}. The voltages achieved in alkaline freshwater (1 M KOH) and alkaline seawater (1 M KOH + Natural Seawater) electrolytes are comparable, and both sets of voltages are even better than those previously reported for other catalyst systems, as illustrated in Fig. 4C.[56–69] In order to study the selectivity of Fe–CoCr LDH toward the OER in seawater, we evaluated the Faradaic efficiency at 500 mA cm^{-2} in 1 M KOH + Natural Seawater using an H-type cell (Fig. S16A). Impressively, as shown in Fig. S16B, the catalyst maintained high Faradaic efficiency, averaging 99.3%, with no detectable hypochlorite formation as verified by a hypochlorite detection test (Fig. S17), highlighting its excellent selectivity for the OER in real seawater environments. In addition to confirming high OER selectivity, these results also provide

insights into the corrosion resistance of the catalyst in alkaline seawater. The absence of chlorine-related byproducts indicates that chloride adsorption and subsequent corrosion pathways are effectively suppressed under operating conditions. Previous studies have shown that transition-metal oxyhydroxides generated $in\ situ$ during anodic polarization can act as protective layers, selectively promoting the OER while inhibiting chloride attack.[59] Similarly, Fe incorporation has been reported to facilitate the self-reconstruction of hydroxide phases into robust metal oxyhydroxide layers, which enhance both catalytic activity and chloride tolerance.[70] In our system, the coexistence of CoOOH and Fe-modified CoCr LDH is likely to play a comparable role, where the oxyhydroxide phase not only contributes to OER activity but also improves resistance against chloride-induced degradation. These synergistic effects further substantiate the durability of Fe–CoCr LDH for seawater electrolysis. To further probe its robustness, the Fe–CoCr LDH// NiMoN system was evaluated in 6 M KOH mixed with natural seawater under elevated temperature conditions, which yielded additional enhancements in catalytic activity (Fig. 4D). To gain additional insight into the robustness of Fe–CoCr LDH, we measured its OER activity in 1 M KOH at different temperatures (20, 30, 40, 50, and 60 °C). As shown in Fig. S18A, the polarization curves consistently improve with increasing temperature, and the enhancement is uniform across the entire range without irregular deviations. From these data, an Arrhenius plot was constructed (Fig. S18B), yielding an activation energy that reflects the intrinsic kinetics of the catalyst.[71] This consistent temperature dependence demonstrates that Fe–CoCr LDH maintains stable and predictable catalytic behavior under different operating conditions, underscoring its robustness for practical alkaline OER applications.

Durability was also assessed on the two-electrode system under ambient conditions, where the cell maintained stable operation for 200 hours at 500 mA cm^{-2} followed by another 150 hours at 1000 mA cm^{-2} (Fig. 4E). Complementary long-term tests at 40 °C in the same electrolyte further confirmed its resilience, as the electrode pair sustained 500 mA cm^{-2} for 150 hours with negligible degradation (Fig. 4F).

Conclusions

In summary, we have successfully synthesized an efficient Fe-modified CoCr LDH catalyst on Ni foam by using a Co MOFs precursor and a straightforward post-synthesis modification method. The Fe–CoCr LDH catalyst was found to maintain low overpotentials across a range of current densities in various alkaline electrolytes, including simulated and natural seawater, showcasing its versatility and robustness. Electrochemical impedance spectroscopy further highlighted the enhanced charge transfer kinetics attributed to Fe modification. Moreover, the catalyst demonstrated remarkable long-term stability under harsh conditions, including concentrated alkaline seawater. By coupling Fe–CoCr LDH with a good HER counterpart, we achieved efficient overall water splitting performance in a

two-electrode system with low cell voltages at high current densities in multiple electrolytes and good stability for over 350 hours at industrially relevant current densities. This work provides insights into the design of earth-abundant, non-precious metal catalysts with superior electrocatalytic properties, advancing the development of cost-effective and scalable solutions for green hydrogen production.

Conflicts of interest

There are no conflicts of interest to declare.

Data availability

The data supporting this article have been included as part of the supplementary information (SI). Supplementary information: experimental details and results. See DOI: https://doi.org/10.1039/d5ey00267b.

Acknowledgements

References

1 F. Yu, L. Yu, I. K. Mishra, Y. Yu, Z. Ren and H. Zhou, *Mater. Today Phys.*, 2018, **7**, 121–138.

2 J. Kibsgaard and I. Chorkendorff, *Nat. Energy*, 2019, **4**, 430–433.

3 D. Young Chung, P. P. Lopes, P. Farinazzo Bergamo Dias Martins, H. He, T. Kawaguchi, P. Zapol, H. You, D. Tripkovic, D. Strmcnik, Y. Zhu, S. Seifert, S. Lee, V. R. Stamenkovic and N. M. Markovic, *Nat. Energy*, 2020, **5**, 222–230.

4 Z. Y. Yu, Y. Duan, X. Y. Feng, X. Yu, M. R. Gao and S. H. Yu, *Adv. Mater.*, 2021, **33**, 2007100.

5 R. Roy, G. Antonini, K. S. Hayibo, M. M. Rahman, S. Khan, W. Tian, M. S. H. Boutilier, W. Zhang, Y. Zheng, A. Bassi and J. M. Pearce, *Int. J. Hydrogen Energy*, 2025, **116**, 200–210.

6 M. K. Singla, J. Gupta, S. Beryozkina, M. Safaraliev and M. Singh, *Int. J. Hydrogen Energy*, 2024, **61**, 664–677.

7 A. Ajanovic, M. Sayer and R. Haas, *Int. J. Hydrogen Energy*, 2022, **47**, 24136–24154.

8 Z. Hammi, N. Labjar, M. Dalimi, Y. El Hamdouni, E. M. Lotfi and S. El Hajjaji, *Int. J. Hydrogen Energy*, 2024, **80**, 1030–1045.

9 L. Peng, N. Yang, Y. Yang, Q. Wang, X. Xie, D. Sun-Waterhouse, L. Shang, T. Zhang and G. I. N. Waterhouse, *Angew. Chem., Int. Ed.*, 2021, **60**, 24612–24619.

10 J. Wang, X. Li, H. Liang, C. Zhang, H. Du, Y. Sun, H. Li, H. Pan, Y. Hao, M. Zhao, T. Li and T. Ma, *Adv. Funct. Mater.*, 2025, 2503596.

11 M. Li, D. Ma, X. Feng, C. Zhi, Y. Jia, J. Zhang, Y. Zhang, Y. Chen, L. Shi and J. W. Shi, *Small*, 2025, **21**, 2412576.

12 Y. Yuan, Y. Yang, G. Liu, M. Chang, Z. Liu, K. Gao, H. Zheng, M. Ye and J. Shen, *Adv. Funct. Mater.*, 2025, **35**, 2422889.

13 R. Zhang, Q. Wu, Y. Han, Y. Zhang, X. Wu, J. Zeng, K. Huang, A. Du, J. Chen, D. Zhou and X. Yao, *Small*, 2025, **21**, 2408266.

14 F. Wu, F. Tian, M. Li, S. Geng, L. Qiu, L. He, L. Li, Z. Chen, Y. Yu, W. Yang and Y. Hou, *Angew. Chem., Int. Ed.*, 2025, **64**, e202413250.

15 G. Li, L. Li, J. Zhang, S. Shan, C. Yuan and T. C. Weng, *ChemSusChem*, 2024, **18**, e202401582.

16 Y. Yao, C. Zou, S. Sun, Y. Guo, S. Hong, Z. Cai, C. Yang, W. Zhuang, F. Luo, M. S. Hamdy, F. A. Ibrahim, F. Gong, Y. Li, X. Sun and W. Hu, *Small*, 2025, **21**, 2409627.

17 F. Dionigi, T. Reier, Z. Pawolek, M. Gliech and P. Strasser, *ChemSusChem*, 2016, **9**, 962–972.

18 S. Dresp, F. Dionigi, M. Klingenhof and P. Strasser, *ACS Energy Lett.*, 2019, **4**, 933–942.

19 P. Farràs, P. Strasser and A. J. Cowan, *Joule*, 2021, **5**, 1921–1923.

20 H. Jin, J. Xu, H. Liu, H. Shen, H. Yu, M. Jaroniec, Y. Zheng and S.-Z. Qiao, *Sci. Adv.*, 2023, **9**, eadi7755.

21 J. Chang, G. Wang, Z. Yang, B. Li, Q. Wang, R. Kuliiev, N. Orlovskaya, M. Gu, Y. Du, G. Wang and Y. Yang, *Adv. Mater.*, 2021, **33**, 2101425.

22 L. Yu, J. Xiao, C. Huang, J. Zhou, M. Qiu, Y. Yu, Z. Ren, C. W. Chu and J. C. Yu, *Proc. Natl. Acad. Sci. U. S. A.*, 2022, **119**, e2202382119.

23 Y. Liu, Y. Wang, P. Fornasiero, G. Tian, P. Strasser and X. Y. Yang, *Angew. Chem., Int. Ed.*, 2024, **63**, e202412087.

24 L. Wang, D. Wang, L. Zheng, X. Song, Y. Yan, J. Li, S. Tian, M. Wang, M. Peng, Z. Yin, H. Wang, J. Xu, B. Cheng, Z. Yin and D. Ma, *Nano Res.*, 2024, **17**, 9472–9482.

25 B. Zhang, Y. Zheng, T. Ma, C. Yang, Y. Peng, Z. Zhou, M. Zhou, S. Li, Y. Wang and C. Cheng, *Adv. Mater.*, 2021, **33**, 2006042.

26 T. Ibomcha Singh, G. Rajeshkhanna, U. Narayan Pan, T. Kshetri, H. Lin, N. Hoon Kim and J. Hee Lee, *Small*, 2021, **17**, 2101312.

27 A. Bereketova, M. Nallal, M. Yusuf, S. Jang, K. Selvam and K. H. Park, *RSC Adv.*, 2021, **11**, 16823–16833.

28 S. He, T. Jiang, C. Ye, W. Wang and S. Tang, *J. Colloid Interface Sci.*, 2025, **695**, 137749.

29 Z. Lv, H. Zhang, C. Liu, S. Li, J. Song and J. He, *Adv. Sci.*, 2024, **11**, 2306678.

30 Y. Guo, Q. Huang, J. Ding, L. Zhong, T. T. Li, J. Pan, Y. Hu, J. Qian and S. Huang, *Int. J. Hydrogen Energy*, 2021, **46**, 22268–22276.

31 C. Dong, X. Yuan, X. Wang, X. Liu, W. Dong, R. Wang, Y. Duan and F. Huang, *J. Mater. Chem. A*, 2016, **4**, 11292–11298.

32 B. Malik, H. K. Sadhanala, S. K. T. Aziz, S. Majumder, R. Konar, A. Gedanken and G. D. Nessim, *ACS Appl. Nano Mater.*, 2022, **5**, 4091–4101.

33 C. Dong, X. Zhang, J. Xu, R. Si, J. Sheng, J. Luo, S. Zhang, W. Dong, G. Li, W. Wang and F. Huang, *Small*, 2020, **16**, 1905328.

34 S. Khatun and P. Roy, *Chem. Commun.*, 2022, **58**, 1104–1107.

35 K. Zhu, J. Chen, W. Wang, J. Liao, J. Dong, M. O. L. Chee, N. Wang, P. Dong, P. M. Ajayan, S. Gao, J. Shen and M. Ye, *Adv. Funct. Mater.*, 2020, **30**, 2003556.

36 H. Chen, Z. Shen, Z. Pan, Z. Kou, X. Liu, H. Zhang, Q. Gu, C. Guan and J. Wang, *Adv. Sci.*, 2019, **6**, 1802002.

37 X. Zhang, F. Yan, X. Ma, C. Zhu, Y. Wang, Y. Xie, S. L. Chou, Y. Huang and Y. Chen, *Adv. Energy Mater.*, 2021, **11**, 2102141.

38 C. Luan, M. Corva, U. Hagemann, H. Wang, M. Heidelmann, K. Tschulik and T. Li, *ACS Catal.*, 2023, **13**, 1400–1411.

39 W. H. Lee, M. H. Han, Y. J. Ko, B. K. Min, K. H. Chae and H. S. Oh, *Nat. Commun.*, 2022, **13**, 605.

40 X. Zhang, H. Zhong, Q. Zhang, Q. Zhang, C. Wu, J. Yu, Y. Ma, H. An, H. Wang, Y. Zou, C. Diao, J. Chen, Z. G. Yu, S. Xi, X. Wang and J. Xue, *Nat. Commun.*, 2024, **15**, 1383.

41 S. Niu, W. J. Jiang, T. Tang, L. P. Yuan, H. Luo and J. S. Hu, *Adv. Funct. Mater.*, 2019, **29**, 1902180.

42 F. Yang, Y. Chen, G. Cheng, S. Chen and W. Luo, *ACS Catal.*, 2017, **7**, 3824–3831.

43 M. C. Biesinger, B. P. Payne, A. P. Grosvenor, L. W. M. Lau, A. R. Gerson and R. S. C. Smart, *Appl. Surf. Sci.*, 2011, **257**, 2717–2730.

44 S. P. Babu and A. Falch, *ChemCatChem*, 2022, **14**, e202200364.

45 M. Schindler, F. C. Hawthorne, M. S. Freund and P. C. Burns, *Geochim. Cosmochim. Acta*, 2009, **73**, 2488–2509.

46 R. Dudric, A. Vladescu, V. Rednic, M. Neumann, I. G. Deac and R. Tetean, *J. Mol. Struct.*, 2014, **1073**, 66–70.

47 Y. Duan, Z. Y. Yu, S. J. Hu, X. S. Zheng, C. T. Zhang, H. H. Ding, B. C. Hu, Q. Q. Fu, Z.-L. Yu, X. Zheng, J. F. Zhu, M. R. Gao and S. H. Yu, *Angew. Chem., Int. Ed.*, 2019, **58**, 15772–15777.

48 M. S. Burke, M. G. Kast, L. Trotochaud, A. M. Smith and S. W. Boettcher, *J. Am. Chem. Soc.*, 2015, **137**, 3638–3648.

49 E. M. Davis, A. Bergmann, H. Kuhlenbeck and B. R. Cuenya, *J. Am. Chem. Soc.*, 2024, **146**, 13770–13782.

50 F. Dionigi, Z. Zeng, I. Sinev, T. Merzdorf, S. Deshpande, M. B. Lopez, S. Kunze, I. Zegkinoglou, H. Sarodnik, D. Fan, A. Bergmann, J. Drnec, J. F. de Araujo, M. Gliech, D. Teschner, J. Zhu, W.-X. Li, J. Greeley, B. R. Cuenya and P. Strasser, *Nat. Commun.*, 2020, **11**, 2522.

51 T. Ha, T.-H. Shen, Y. Ko, L. Zhong, L. Lombardo, W. Luo, S. Horike, V. Tileli and A. Züttel, *J. Am. Chem. Soc.*, 2023, **145**, 23691–23701.

52 J. Baek, M. D. Hossain, P. Mukherjee, J. Lee, K. T. Winther, J. Leem, Y. Jiang, W. C. Chueh, M. Bajdich and X. Zheng, *Nat. Commun.*, 2023, **14**, 5936.

53 T. Zhang, H.-F. Zhao, Z.-J. Chen, Q. Yang, N. Gao, L. Li, N. Luo, J. Zheng, S.-D. Bao, J. Peng, X. Peng, X.-W. Liu and H.-B. Yu, *Nat. Commun.*, 2025, **16**, 3327.

54 H. Chen, P. Liu, W. Li, W. Xu, Y. Wen, S. Zhang, L. Yi, Y. Dai, X. Chen, S. Dai, Z. Tian, L. Chen and Z. Lu, *Adv. Mater.*, 2024, **36**, 2411302.

55 S. Zhang, Y. Wang, S. Li, Z. Wang, H. Chen, L. Yi, X. Chen, Q. Yang, W. Xu, A. Wang and Z. Lu, *Nat. Commun.*, 2023, **14**, 4822.

56 S. Pal, K. Shimizu, S. Khatun, S. Singha, S. Watanabe and P. Roy, *J. Mater. Chem. A*, 2023, **11**, 12151–12163.

57 F. Sun, Y. Wang, X. Tian, R. Zhu, Z. Zhuang, Y. Zheng, J. Zang and L. Dong, *Chem. Eng. J.*, 2024, **499**, 156680.

58 S. Pan, R. Li, J. Wang, Q. Zhang, M. Wang, B. Shi, P. Wang, Y. Zhao and X. Zhang, *ACS Nano*, 2023, **17**, 4539–4550.

59 L. Yu, Q. Zhu, S. Song, B. McElhenny, D. Wang, C. Wu, Z. Qin, J. Bao, Y. Yu, S. Chen and Z. Ren, *Nat. Commun.*, 2019, **10**, 5106.

60 L. Wu, L. Yu, F. Zhang, B. McElhenny, D. Luo, A. Karim, S. Chen and Z. Ren, *Adv. Funct. Mater.*, 2021, **31**, 2006484.

61 C. Wang, M. Zhu, Z. Cao, P. Zhu, Y. Cao, X. Xu, C. Xu and Z. Yin, *Appl. Catal., B*, 2021, **291**, 120071.

62 J. Liu, X. Liu, H. Shi, J. Luo, L. Wang, J. Liang, S. Li, L. M. Yang, T. Wang, Y. Huang and Q. Li, *Appl. Catal., B*, 2022, **302**, 120862.

63 Y. Shi, S. Zhou, J. Liu, X. Zhang, J. Yin, T. Zhan, Y. Yang, G. Li, J. Lai and L. Wang, *Appl. Catal., B*, 2024, **341**, 123326.

64 J. Chen, B. Ren, H. Cui and C. Wang, *Small*, 2020, **16**, 1907556.

65 X. Wang, X. Han, R. Du, C. Xing, X. Qi, Z. Liang, P. Guardia, J. Arbiol, A. Cabot and J. Li, *ACS Appl. Mater. Interfaces*, 2022, **14**, 41924–41933.

66 L. Wu, L. Yu, B. McElhenny, X. Xing, D. Luo, F. Zhang, J. Bao, S. Chen and Z. Ren, *Appl. Catal., B*, 2021, **294**, 120256.

67 D. Senthil Raja, X. F. Chuah and S. Y. Lu, *Adv. Energy Mater.*, 2018, **8**, 1801065.

68 Q. Wang, X. Du and X. Zhang, *Int. J. Hydrogen Energy*, 2023, **48**, 9260–9272.

69 K. Jiang, W. Liu, W. Lai, M. Wang, Q. Li, Z. Wang, J. Yuan, Y. Deng, J. Bao and H. Ji, *Inorg. Chem.*, 2021, **60**, 17371–17378.

70 C. Huang, Q. Zhou, D. Duan, L. Yu, W. Zhang, Z. Wang, J. Liu, B. Peng, P. An, J. Zhang, L. Li, J. Yu and Y. Yu, *Energy Environ. Sci.*, 2022, **15**, 4647–4658.

71 L. Wu, M. Ning, X. Xing, Y. Wang, F. Zhang, G. Gao, S. Song, D. Wang, C. Yuan, L. Yu, J. Bao, S. Chen and Z. Ren, *Adv. Mater.*, 2023, **35**, 2306097.